Superconductivity in monocrystalline $YNiSi_3$ and $LuNiSi_3$

Fabiana R. Arantes,[1] Deisy Aristizábal-Giraldo,[1,2] Daniel A. Mayoh,[3] Yu Yamane,[4] Chongli Yang,[4] Martin R. Lees,[3] Jorge M. Osorio-Guillén,[2] Toshiro Takabatake,[4] and Marcos A. Avila[1]

[1]*CCNH, Universidade Federal do ABC (UFABC), Santo André, São Paulo, Brazil*

[2]*Instituto de Física, Universidad de Antioquia UdeA, Calle 70 No 52-21, Medellín, Colombia*

[3]*Department of Physics, University of Warwick, Coventry CV4 7AL, United Kingdom*

[4]*Graduate School of Advanced Sciences of Matter, Hiroshima University, Higashi-Hiroshima 739-8530, Japan*

(Received 25 July 2018; revised manuscript received 28 March 2019; published 11 June 2019)

We report the discovery of bulk superconductivity in the ternary intermetallics $YNiSi_3$ and $LuNiSi_3$. High-quality single crystals were grown via the Sn-flux method and studied using magnetization, specific-heat, and resistivity measurements at low temperatures. The critical temperatures obtained from these different techniques are in very good agreement and yield $T_c = 1.36(3)$ K and $T_c = 1.61(2)$ K for $YNiSi_3$ and $LuNiSi_3$, respectively. Magnetization measurements indicate that both compounds are among the rare cases where type-I superconductivity occurs in a ternary intermetallic, however, the jump in the specific heat at the transition is lower than the value expected from BCS theory ($\Delta C_{el}/\gamma_n T_c = 1.43$) in both materials and is equal to 1.14(9) and 0.71(5) for the Y and Lu compounds, respectively. Resistivity measurements exhibit sharp transitions but with critical fields $\mu_0 H_c(0)$ ($\approx$0.05 T for $YNiSi_3$ and $\approx$0.08 T for $LuNiSi_3$) considerably higher than those obtained from the magnetization and specific heat ($\approx$0.01 T). First-principles density functional theory calculated electronic structure shows that these compounds have highly anisotropic and complex Fermi surfaces with one electronic and two holelike branches. One hole branch and the electron branch have a large cylindrical topology connecting the first Brillouin-zone boundaries, the former being built up by the hybridization of Y(Lu) d, Ni d, and Si p states, and the latter being built up by Ni d and Si p states. The calculated phononic structures indicate that the coupling of the Y(Lu), Ni d, and Si p electrons in the low-lying optical phonon branches is responsible for the formation of Cooper pairs and the observed superconducting state. Therefore, these compounds can be classified as anisotropic three-dimensional metals with multiband superconducting ground states in the weak-coupling regime.

DOI: 10.1103/PhysRevB.99.224505

I. INTRODUCTION

The search for new superconductors (SCs) has, in the past decade, often focused on heavy-fermion materials and/or materials whose unit cells lack a center of inversion—the noncentrosymmetric (NCS) superconductors [1]. This is because these materials are thought to be good candidates for unconventional superconductors, which do not conform to the Bardeen-Cooper-Schrieffer (BCS) theory [2–5] and can exhibit high critical fields—on the order of a few teslas—as well as high critical temperatures. Despite the large number of reported studies, the relationship between a material's crystal structure and its superconducting properties is not yet firmly established. Therefore, it is essential to explore unusual features of centrosymmetric superconductors in order to unravel the role of crystalline structure *per se*. In the same way, the study of compounds with weak electron correlations, such as Sc-, Y-, La-, and Lu-based SCs, can enhance our comprehension of heavy-fermion SCs.

Superconductors are traditionally categorized into type I or II, according to the transition of the superconducting phase to the normal state under an applied magnetic field: type-I SCs have a Ginzburg-Landau (GL) parameter $\kappa < 1/\sqrt{2}$ and undergo a first-order transition into the superconducting state in a magnetic field, whereas type-II SCs present a second-order phase transition and $\kappa > 1/\sqrt{2}$. The ratio $\kappa = \lambda/\xi$ connects the two length parameters yielded by the GL equations: the GL penetration depth λ and the superconducting coherence length ξ. Within this classification, type-I superconductivity is normally displayed by elemental SCs, e.g., Pb, Hg, and Sn, although several exceptions have been found, such as the binary compounds $CaBi_2$ [6], KBi_2 [7], $ScGa_3$, $LuGa_3$ [8], $YbSb_2$ [9], and $PdTe_2$ [10], the ternary cage compound $LaTi_2Al_{20}$ [11], and the NCS $LaPdSi_3$ [12], and $LaIrSi_3$ [13].

Whereas the vast majority of superconducting binary and ternary intermetallic compounds are of type II, increasing numbers of materials have been found with intermediate behaviors. Therefore, type-II SCs were further classified into types-II/1 ($\kappa \approx 1/\sqrt{2}$), -II/2 (traditional type-II $\kappa > 1/\sqrt{2}$) [14], and -1.5 ($\kappa \gg 1/\sqrt{2}$) [15–17]. Some examples of type II/1 are Nb [18], ZrB_{12} [19,20], and the noncentrosymmetric superconductors AuBe [21], RhGe [22], and $LaRhSi_3$ [23–26]. Type-1.5 SCs may include MgB_2 [15–17] and Sr_2RuO_4 [27].

In the $RNiGe_3$ (R = Y, Ce) (where R represents rare earth) series [28,29] with a centrosymmetric orthorhombic structure, the compounds $YNiGe_3$ [30] and $CeNiGe_3$ [31–33] are superconductors. The former has an unusually low specific heat jump at the transition compared to the prediction of BCS theory [30], whereas the latter is an unconventional heavy-fermion superconductor under pressure.

In this paper, we present a detailed characterization of two nonmagnetic compounds of the RNiSi$_3$ series (those with R = Y, Lu) expected to show many of the same features as YNiGe$_3$ with $T_c = 0.46$ K [30]. We report on the discovery, via resistivity, magnetization, and specific-heat measurements, of bulk type-I superconductivity in single crystals of YNiSi$_3$ and LuNiSi$_3$ with critical temperatures $T_c = 1.36(3)$ K for YNiSi$_3$ and $T_c = 1.61(2)$ K for LuNiSi$_3$. We also present density functional theory (DFT) calculations to obtain the electronic properties of these compounds.

II. METHODS

YNiSi$_3$ and LuNiSi$_3$ single crystals were synthesized via the Sn-flux method originally used to grow YbNiSi$_3$ [34]. A proportion of 1:1:3:45 (Y/Lu:Ni:Si:Sn) was used as detailed in previous work [35] wherein the crystalline structures were verified by powder x-ray diffraction (PXRD) analysis and wavelength dispersive electron-probe microanalysis (EPMA) of the single crystals, conducted in a JEOL JXA-8200 microanalyzer. The crystal compositions were determined by averaging over ten different points of a polished sample.

Resistivity between 0.04 and 4 K was measured with a standard four-probe ac method in a homemade system inside a commercial Cambridge Magnetic Refrigeration mFridge mF-ADR50 with applied magnetic fields in two orientations: parallel or perpendicular to the crystal plate main surfaces. Specific heat between 0.37 and 5 K was measured on crystals with total mass of about 7 mg, under applied fields parallel to the plates, using the 2τ thermal relaxation method in the Quantum Design Physical Property Measurement System.

Magnetic susceptibility was measured in a Quantum Design Magnetic Property Measurement System magnetometer with an iQuantum ^{3}He insert—in this case, the field was perpendicular to the plate surfaces. Proper evaluation of the magnetization measurements in SCs must take into account the demagnetization factor (N) due to the sample shape since the volumetric susceptibility of a bulk SC must approach $\chi \sim -1$ below the critical temperature. In our case, the platelike shape of the crystal made it simple to estimate $N \sim 0.5$ for YNiSi$_3$ and $N \sim 0.7$ for LuNiSi$_3$ with the magnetic field applied perpendicular to the main surface of the sample ($H \parallel b$).

Spin-polarized first-principles DFT calculations, including spin-orbit coupling (SOC) in a second-variational scheme, have been carried out using the full-potential augmented-plane wave method with local orbitals (FP-APW + lo) as implemented in the ELK code [36]. For the exchange-correlation energy functional, we have used the generalized gradient approximation and its PBEsol parametrization [37]. The muffin-tin (MT) radii of Y, Lu, Ni, and Si are set to $R_{MT}^{Y} = 2.7777$, $R_{MT}^{Lu} = 2.7495$, $R_{MT}^{Ni} = 2.0563$, and $R_{MT}^{Si} = 2.0563$ a.u., respectively. The parameter $R_{MT}|\mathbf{G} + \mathbf{k}|_{max}$ governing the number of plane waves in the FP-APW + lo method is chosen to be 9.5. The Brillouin zone (BZ) is sampled with a uniformly spaced $\mathbf{k}$ grid of $8 \times 8 \times 8$ for the structural relaxation and $16 \times 16 \times 16$ for the calculation of the dispersion relation $E(\mathbf{k})$, the total and site projected densities of states (DOS) and the Fermi surface (FS).

III. EXPERIMENTAL RESULTS

Previous work on the series RNiSi$_3$ [35] showed, by PXRD analysis, that these compounds crystallize in the orthorhombic space group *Cmmm*. The experimental lattice constants are given in Table I of the Supplemental Material [38]. Elemental analysis using EPMA revealed average sample compositions of $Y_{0.96(11)}Ni_{1.00(19)}Si_{3.09(18)}$ and $Lu_{1.00(1)}Ni_{0.68(2)}Si_{3.13(2)}$ with an upper limit of ~500 ppm Sn impurities in both crystals. LuNiSi$_3$ crystals thus form with significant Ni vacancies, as observed in the RNiGe$_3$ series [28]. This effect is small for YNiGe$_3$ but is more pronounced for heavier rare earths as in the case of LuNiGe$_3$. There were some small NiSi$_2$ crystallites attached to the surface of the crystals (a diamagnetic non-superconducting metallic silicide [39–41]) that could be easily removed by polishing. Besides Sn ($T_c = 3.7$ K), no other superconducting impurity was detected, so we may claim that the superconducting transitions presented below are due to these new intermetallic compounds.

In the following sections, we describe the characteristics of the superconductivity in YNiSi$_3$ and LuNiSi$_3$ through magnetization, specific-heat, and resistivity experiments.

A. YNiSi$_3$

Figure 1 shows the magnetic characterization of YNiSi$_3$.$\chi(T)$ [Fig. 1(a)] was measured under an applied field of $\mu_0 H = 2$ mT following a zero-field-cooled warming protocol. At 1.31(2) K, there is a relatively sharp transition with χ rising from the value of -1 as expected by the complete field expulsion of a bulk SC. Figure 1(b) shows the $M(H)$ curves at several temperatures below the superconducting transition. They are marked by a type-I SC behavior with $M = -H$ at low fields and an abrupt jump at H_c. The transition in some type-I SC can be broadened by the presence of impurities, inhomogeneities, and even a high demagnetization effect, however the type-I behavior of this sample is very clear, attesting to the quality of the crystal.

The critical fields extracted from the curves in Fig. 1(b) were used to plot the phase diagram displayed in Fig. 1(c). The points were fitted by the empirical parabolic law [42],

$$H_c(T) = H_c(0)\left[1 - \left(\frac{T}{T_c}\right)^2\right], \quad (1)$$

yielding an estimated critical field $\mu_0 H_c(0) = 9.6(2)$ mT.

Figure 2(a) shows the dependence of the total heat-capacity (C_p) on T for YNiSi$_3$ at zero field and with H ranging from 5 mT up to 1 T, a field well above that in which the superconductivity is suppressed. At zero field, there is a jump at 1.35(5) K, agreeing with the bulk superconductivity observed in the magnetization measurements. The data also seem to show a double peak, which could be a sign of a double transition over a narrow temperature range, but the resolution is not sufficient to allow a definitive conclusion. For the curves measured under applied fields, the transition temperature shifts to lower T with values comparable to the critical temperatures observed in Fig. 1(b). The jumps in $C_p(T)$ in 5 and 6 mT are higher than in zero field, suggesting a first-order transition for $H \neq 0$. Figure 2(b) shows the dependence of C_p/T with T for the same data displayed in

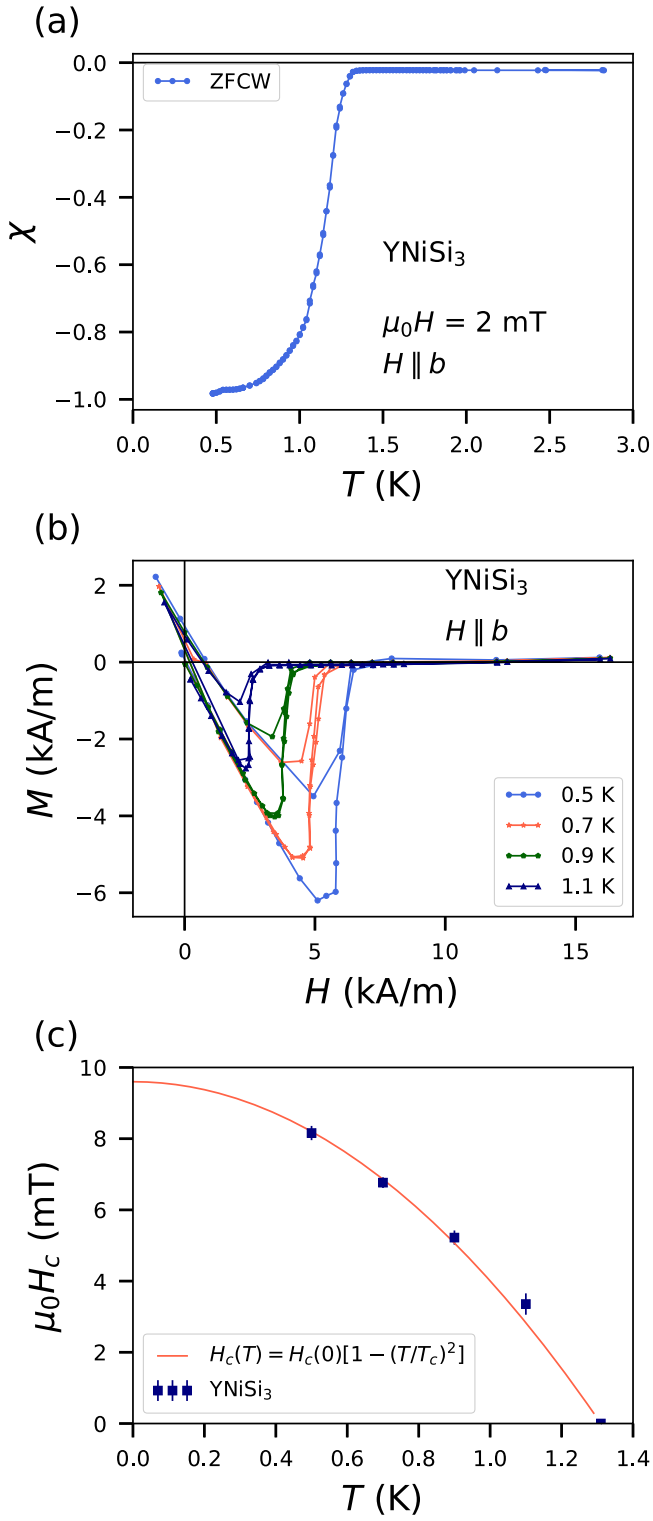

FIG. 1. Magnetization measurements for $YNiSi_3$. (a) Temperature dependence of χ with $\mu_0 H = 2$ mT using a zero-field-cooled warming (ZFCW) protocol. (b) $M(H)$ curves at several temperatures below the superconductor transition. (c) H_c vs T phase diagram with each $H_c(T)$ value extracted from the curves in (b) and the fit made using Eq. (1).

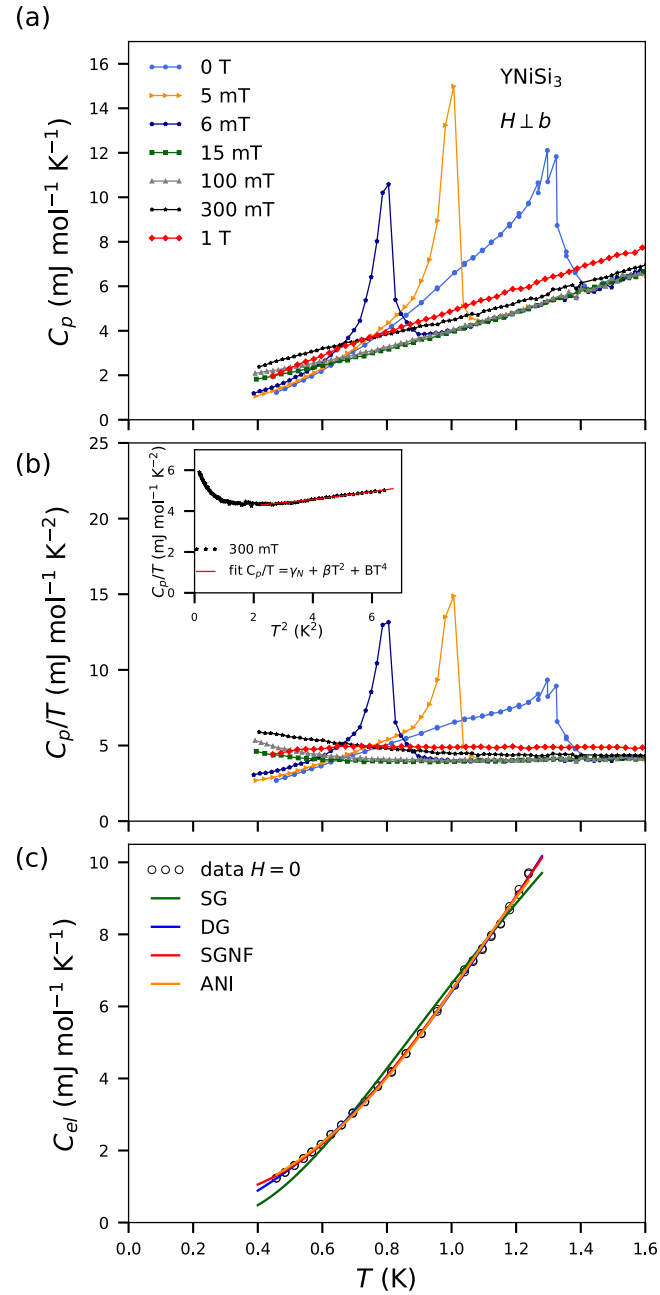

FIG. 2. (a) Temperature dependence of C_p at several magnetic fields for $YNiSi_3$. (b) C_p/T vs T for the same curves displayed in Fig. 2(a). The inset shows C_p/T vs T^2 for a larger range of temperature. (c) Electronic contribution of specific heat for $H = 0$ with the fits obtained with the models given in Eqs. (5) and (6).

Fig. 2(a), whereas the inset shows C_p/T vs T^2 measured with $\mu_0 H = 300$ mT. The normal-state C_p was fit with the expression $C_p(T)/T = \gamma_N + \beta T^2 + BT^4$ where the first term is due to the electronic contribution and the $\beta T^2 + BT^4$ terms describe the phonon contribution following the Debye model. The fit yields $\gamma_N = 4.04(9)$ mJ mol^{-1} K^{-2}, $\beta = 0.0961(5)$ mJ mol^{-1} K^{-4}, and $B = 0.0090(5)$ mJ mol^{-1} K^{-6}. The Debye temperature can be evaluated using

$$\theta_D = \left(\frac{n 12\pi^4 R}{5\beta}\right)^{1/3}, \tag{2}$$

where $n = 5$ is the number of atoms per formula unit and R is the molar gas constant, yielding $\theta_D = 466(9)$ K. The values of γ_N and θ_D are comparable to those obtained in the previous work at high temperatures $\gamma_N = 4.1$ mJ mol^{-1} K^{-2} and $\theta_D = 393$ K [35]. The density of states at the Fermi-level $[N(E_F)]$ is obtained using the relation,

$$N(E_F) = \frac{3\gamma_N}{\pi^2 k_B^2 N_A}, \tag{3}$$

where k_B is the Boltzmann constant and N_A is the Avogadro number, resulting in $N(E_F) = 1.71$ states/eV f.u. The electron-phonon coupling constant $\lambda_{e\text{-}ph}$ is calculated using McMillan's formula [43],

$$\lambda_{e\text{-}ph} = \frac{1.04 + \mu^* \ln(\theta_D/1.45T_c)}{(1 - 0.62\mu^*)\ln(\theta_D/1.45T_c) - 1.04}, \tag{4}$$

where μ^* is usually taken between 0.1 and 0.15. Using a μ^* of 0.125 yields $\lambda_{e\text{-}ph} = 0.43(2)$ placing $YNiSi_3$ in the weak-coupling regime together with the NCS $LaPdSi_3$ [12], ($\lambda_{e\text{-}ph} = 0.51$) $LaRhSi_3$ [24] ($\lambda_{e\text{-}ph} = 0.5$), and Th_7Fe_3 ($\lambda_{e\text{-}ph} = 0.59$) [44]. It should be noted that McMillan's formula works better for pure metals because the Debye temperature is not properly defined in compounds containing elements with such large differences in their atomic masses.

Figure 2(c) shows the electronic heat-capacity (C_{el}), obtained by subtracting the $\beta T^3 + BT^5$ terms from the zero-field data. For a BCS superconductor, the jump of ΔC_{el} is expected to have an s-wave gap with $\Delta C_{el}/\gamma_N T_c = 1.43$; however, the estimated value for this compound is 1.14(9), significantly lower than expected. This has also been observed for the ternary type-I SC $LaIrSi_3$ [13] and for the similar compound $YNiGe_3$ [30]; in both cases, it was hypothesized that such a low value of the specific-heat jump is related to a large anisotropy in the superconducting gap.

We have tested four different models to fit the C_{el} data in the superconducting regime: a single-gap α model for a BCS SC (C_{el}^{SG}), a double-gap α model (C_{el}^{DG}), a single-gap α model with a contribution from a nonsuperconducting fraction (C_{el}^{SGNF}), and finally, an anisotropic gap model (C_{el}^{ANI}) in order to verify the hypothesis discussed above. The first three models are given by the equations below,

$$C_{el}^{SG} = A_1 \gamma_N T_c \exp\left(-\Delta_0^{SG}/k_B T\right), \tag{5a}$$

$$C_{el}^{DG} = A_2 \gamma_N T_c \left[f \exp\left(-\Delta_0^{DG1}/k_B T\right) + (1-f)\exp\left(-\Delta_0^{DG2}/k_B T\right)\right], \tag{5b}$$

$$C_{el}^{SGNF} = A_3 \gamma_N T_c \exp\left(-\Delta_0^{SGNF}/k_B T\right) + \gamma_2 T, \tag{5c}$$

where A_i's are scale factors, Δ_0 is the superconducting gap, and f is the superconducting fraction for each gap (DG model). For the anisotropic model, we used the integral form of the $C_{el}(T)$ formula given by BCS theory, and we considered an angular- and temperature-dependent gap $\Delta(T, \theta)$ representing a single extended s-wave gap [2,45,46],

$$C_{el}^{ANI}(T) = A_4 \frac{N(E_F)}{\pi T} \int_0^{2\pi} d\phi \int_0^{\pi} d\theta \, \sin\theta \times \int_0^{\hbar\omega_D} -\frac{\partial f}{\partial E}\left(E^2 + \frac{1}{2}\beta \frac{d\Delta^2(T,\theta)}{d\beta}\right) dE, \tag{6a}$$

$$f = [1 + \exp(\beta E)]^{-1}, \tag{6b}$$

$$\Delta(T, \theta) = \Delta_0(T)(1 + \alpha' \cos 2\theta), \tag{6c}$$

$$\Delta_0(T) = \Delta_0^{ANI} \tanh\left[\left(\pi k_B T_c/\Delta_0^{ANI}\right)\sqrt{a(T_c/T - 1)}\right]. \tag{6d}$$

Here, $\hbar$ is the reduced Planck constant, $\beta = 1/k_B T$, ω_D is the Debye frequency, α' is the anisotropy parameter ($\alpha' = 0$ corresponds to an isotropic s-wave gap) [46], and a is a constant that depends on the coupling strength and the geometry of the gap [47,48].

TABLE I. Fitted parameters of C_{el} in the superconducting region for $YNiSi_3$. A_i, α, and a are dimensionless, Δ_0 is measured in 10^{-23} J, and γ_2 is measured in mJ mol^{-1} K^{-2}.

C_{el} model	A_i	Δ_0	f	γ_2	α'	a
SG	6.7(7)	2.4(1)				
DG	15(1)	1.3(1), 4.5(2)	0.11(1)			
SGNF	10(1)	3.5(2)		2.4(1)		
ANI	0.55(6)	5.4(3)			0.95(9)	0.67(7)

Table I presents the fit parameters for all four models. The simplest model C_{el}^{SG} yielded a poor fit to the data, meaning that the simple s-wave model does not describe this compound well. The three other more complex models fit the data better. Although the quality of the fits is similar, these three models represent distinct physical hypotheses. The double-gap α model assumes that there are two superconducting gaps and can be thought of as a simplified modeling of a more realistic scenario with a distribution of gaps. The α model with a nonsuperconducting fraction, on the other hand, assumes that a fraction of the material is in the normal state due to impurities or other inhomogeneities. And finally, the anisotropic model, as the name suggests, considers a superconducting gap with anisotropy. Given that these are high-quality single-crystal samples, we do not expect a large nonsuperconducting fraction, thus, our results indicate that the superconducting gap is probably not simple, with a magnitude close to 5×10^{-23} J.

Resistivity is not considered a robust technique to characterize a new bulk superconductor because it can be easily affected by impurities that can form a percolation path through which the superconducting current can flow. For this system, the sample used to measure the resistivity had to be carefully chosen and polished due to the presence of small amounts of Sn flux that could mask the compound's transition. In Fig. 3, we show $\rho(T)$ measurements at several applied fields along the directions $H \parallel b$ [Fig. 3(a)] and $H \perp b$ [Fig. 3(b)]. Unfortunately, due to both the geometry of the equipment and the sample, it was not possible to change the direction of the applied field without changing its direction with respect to the

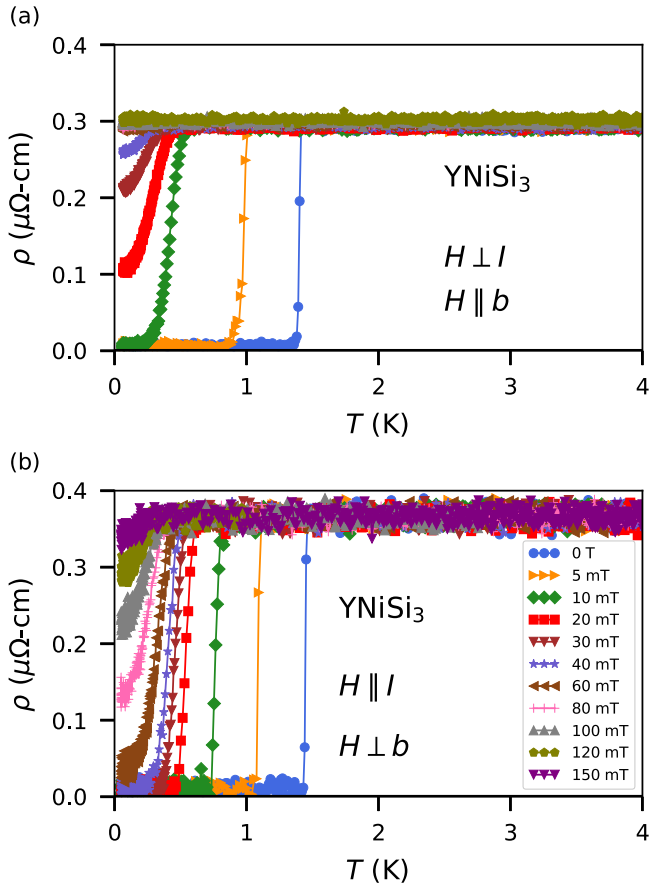

FIG. 3. Temperature dependence of the resistivity for $YNiSi_3$ with H ranging from zero up to 0.15 T. (a) shows the configuration with $H \perp I$ and $H \parallel b$ and (b) with $H \parallel I$ and $H \perp b$.

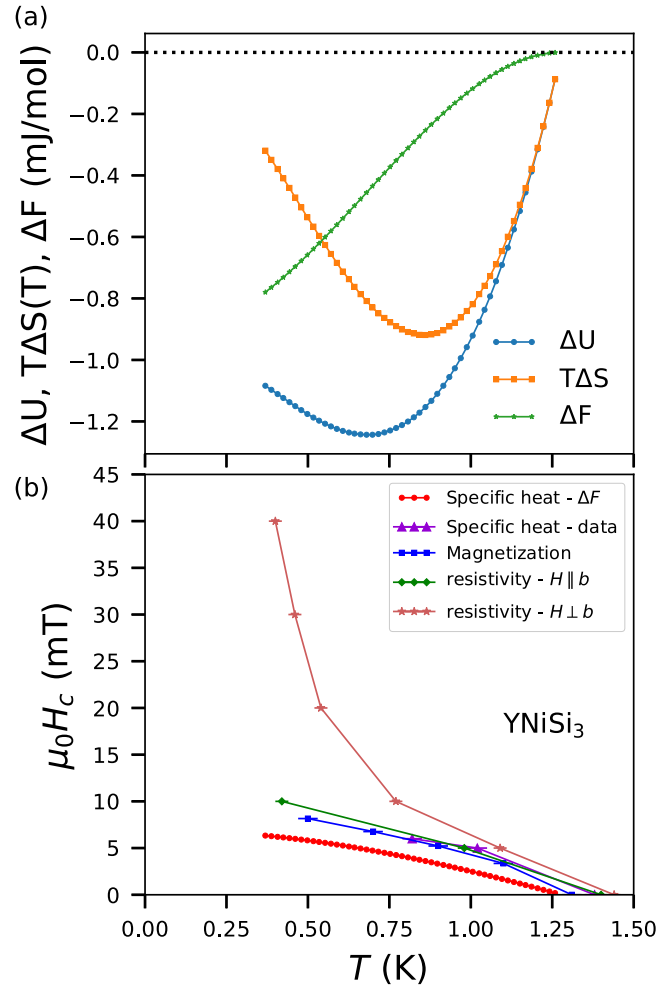

FIG. 4. (a) Temperature dependence of the internal energy difference (ΔU), latent heat ($T\,\Delta S$), and free-energy (ΔF) for $YNiSi_3$. These curves were calculated using the specific-heat measurements at zero field and Eq. (7). (b) Temperature dependence of the critical field $H_c(T)$ obtained from different techniques: using the free energy shown in (a) and the specific-heat, magnetization, and resistivity measurements as a function of the applied field.

current, so a discussion on the presence of any anisotropic magnetoresistance effects is left for future work.

At zero field, there is a sharp transition at 1.42(2) K with $\rho(T)$ quickly reaching zero even with a highest available data point density. The residual resistivity before the superconducting transition is $\rho_0 = 0.33(3)\ \mu\Omega\,\mathrm{cm}$, obtained by averaging the values estimated in both directions, and the residual resistivity ratio (RRR), already published [35], is 54(5). With increasing magnetic field, there is very little broadening of the transition, however, for H higher than 20 mT, the transition is no longer complete. Comparison of Figs. 3(a) and 3(b) indicates that there is an important anisotropy with the configuration displayed in Fig. 3(b) showing higher T_c for the same H and a complete superconducting transition even under the presence of an applied field of 40 mT. Measuring down to 40 mK allows the observation of a partial transition under fields as high as 0.15 T in the configuration shown in Fig. 3(b). The critical fields obtained with these measurements are considerably higher than those observed in the magnetization and specific-heat measurements. We will return to this point in the Discussion section.

The thermodynamic quantities related to the first-order superconducting transition can be evaluated using the zero-field electronic specific-heat data displayed in Fig. 2(c). The equations below give the relationship between the internal energy (ΔU), latent heat ($T\,\Delta S$), free energy (ΔF), and critical field [$H_c(T)$] and how we can evaluate them from the specific-heat data,

$$\begin{aligned}
\Delta F(T) &= -\frac{\mu_0 V H_c^2(T)}{2} = \Delta U - T\,\Delta S,\\
\Delta U(T) &= \int_T^{T_c} [C_s(T') - C_n(T')]dT',\\
\Delta S(T) &= \int_T^{T_c} \frac{C_s(T') - C_n(T')}{T'}dT',
\end{aligned} \tag{7}$$

where V is the volume of a formula unit. Figure 4(a) shows the dependence of ΔU, $T\,\Delta S$, and ΔF with temperature for $YNiSi_3$. The dependence of $H_c(T)$ obtained with this method is displayed in Fig. 4(b) and yields a critical field $\mu_0 H_c(0)$ of 7.0(7) mT, lower than the one obtained from magnetization [Fig. 1(c)]. Along with this curve, we display, in Fig. 4(b), the behavior of $H_c(T)$ for $YNiSi_3$ obtained with the experimental

results presented above, including the data shown in Fig. 1(c). The values of H_c and T_c resulting from the $\rho(T)$ curves were obtained taking the temperature corresponding to a decrease in 50% of ρ_0, and we disregarded the curves that did not reach zero resistivity, although the transitions can be observed with fields as high as 150 mT. Despite all the results pointing to type-I superconductivity, it is notable that the critical fields obtained from resistivity with configuration $H \perp b$ are about eight times higher at low temperatures compared to the other techniques. This could be an effect of surface superconductivity that only $\rho(T)$ can probe, but as it is highly anisotropic, it seems a robust effect.

The techniques discussed above allow us to obtain the basic superconducting parameters for $YNiSi_3$. The electron-density n can be calculated considering the contribution of the three electrons from Y^{3+} and the presence of four formula units per unit cell of the compound ($Z = 4$), yielding $n = 12/V_{\text{cell}} = 3.70 \times 10^{28}$ m^{-3}, where $V_{\text{cell}} = 324.49$ Å^3 for $YNiSi_3$ [35]. Assuming a spherical Fermi surface, k_F is given by $k_F = (3n\pi^2)^{1/3}$ which leads to an effective mass $m^* = \hbar^2 k_F^2 \gamma_N / \pi^2 n k_B^2 = 1.54 m_0$, where m_0 is the free-electron mass and γ_N is in volume units [the density of $YNiSi_3$ is 4.7459(2) g/cm^3]. The mean free path is given by $l = \hbar k_F / n e^2 \rho_0 = 347$ nm. The London penetration depth λ_L can be estimated from the relation $\lambda_L = (m^*/\mu_0 n e^2)^{1/2}$ and is equal to 34(3) nm. Finally, the BCS coherence length in the clean limit is $\xi_0 = 0.18 \hbar^2 k_F / k_B T_c m^* = 780(80)$ nm. Using the relations $\lambda_{GL} = \lambda_L (1 + 0.75\xi_0/l)^{1/2}/\sqrt{2}$ and $\xi_{GL} = 0.74\xi_0(1 + 0.75\xi_0/l)^{-1/2}$ for $T = 0$ [49], we obtain $\kappa = \lambda_{GL}/\xi_{GL} = 0.113(11)$. This value puts $YNiSi_3$ in the type-I limit since $\kappa < 1/\sqrt{2}$, in line with the results from the previous measurements.

B. $LuNiSi_3$

The superconducting properties of $LuNiSi_3$ are very similar to $YNiSi_3$, but the superconductivity occurs at a higher critical temperature [$T_c = 1.61(2)$ K]. As the ionic radius of Lu^{3+} is smaller than Y^{3+}, $LuNiSi_3$ has a smaller unit-cell volume than $YNiSi_3$, confirmed by previous x-ray analysis [35]. This increase in T_c may be a consequence of a chemical pressure effect from the reduced volume, making these compounds good candidates for subsequent low-temperature pressure studies.

Figure 5 shows the magnetic measurements for $LuNiSi_3$ after taking into account the demagnetization factor correction. $\chi(T)$ displayed in Fig. 5(a) was collected using a ZFC-FCW protocol with an applied field of $\mu_0 H = 1$ mT perpendicular to the plate ($H \parallel b$). The transition occurs at 1.58(2) K with $\chi(T)$ approaching -1 at low temperatures. The $M(H)$ curves displayed in Fig. 5(b), at several temperatures below T_c, present the same features of a type-I SC observed for $YNiSi_3$. A fit of the experimental critical field points in the phase diagram [Fig. 5(c)] using Eq. (1) yields $\mu_0 H_c(0) = 10.4(2)$ mT.

The dependence of the specific heat on T at several applied fields for $LuNiSi_3$ is presented in Fig. 6. Figure 6(a) shows a sharp transition at 1.63(2) K in zero field due to the superconducting transition. The transition shifts to lower temperatures with an increasing applied field as expected. The main panel in Fig. 6(b) shows the curve C_p/T vs T, whereas the inset shows C_p/T vs T^2 measured

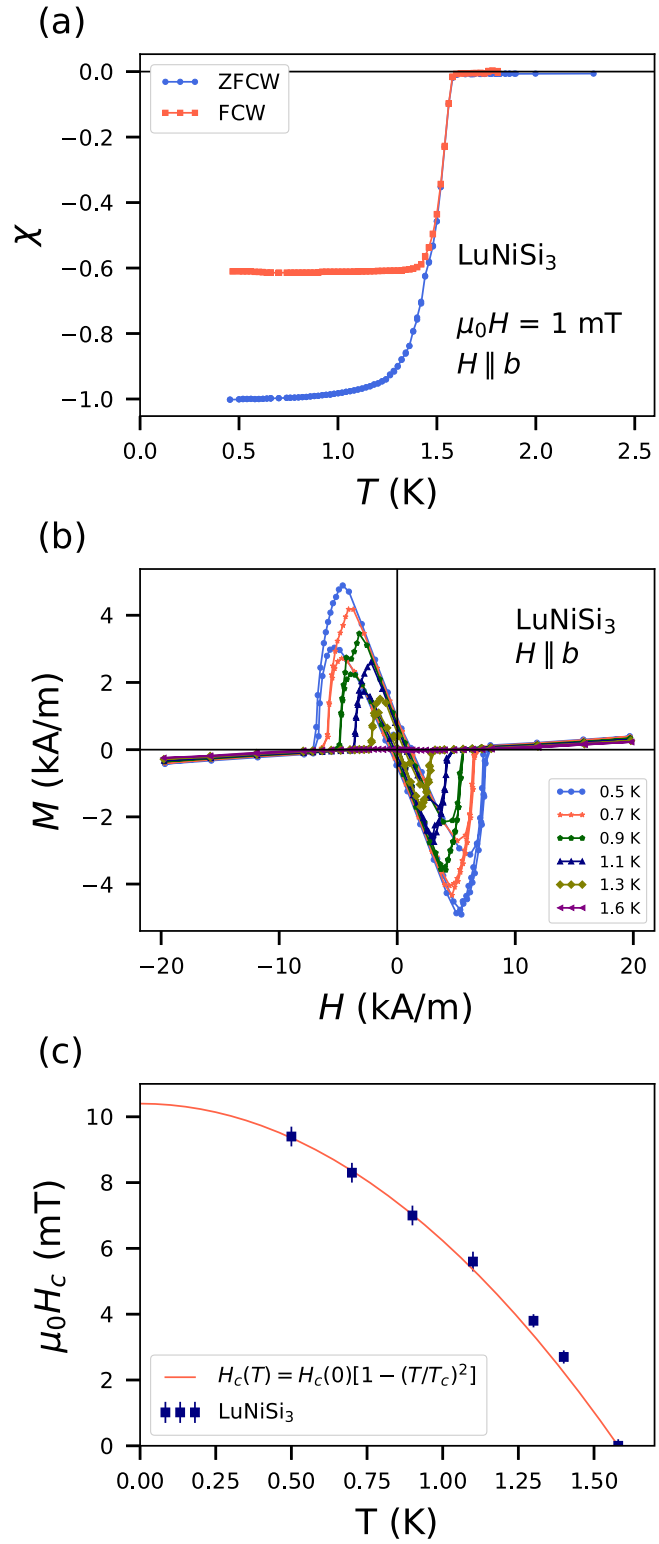

FIG. 5. Magnetization measurements for $LuNiSi_3$. (a) Temperature dependence of χ with $\mu_0 H = 1$ mT using a ZFCW-FCW protocol. (b) $M(H)$ curves at several temperatures below the superconductor transition. (c) Phase diagram with H_c extracted from the curves in panel (b) and the fit of Eq. (1).

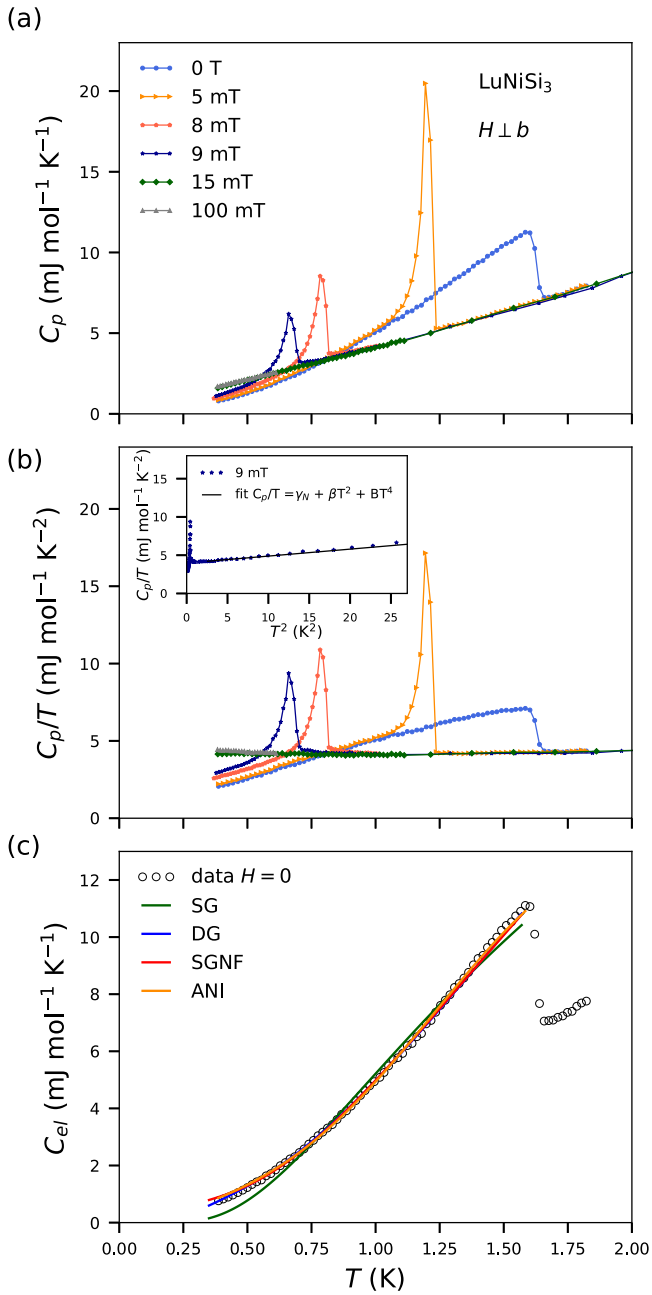

FIG. 6. (a) Temperature dependence of C_p in several magnetic fields for $LuNiSi_3$. (b) C_p/T vs T for the same curves displayed in (a). The inset shows C_p/T vs T^2 for a larger range of temperature. (c) Electronic contribution of specific heat for $H = 0$ with the fits obtained with the models given in Eqs. (5) and (6).

with $\mu_0 H = 9$ mT and the fit above the superconducting transition. The value of $\gamma_N = 3.97(9)$ mJ mol^{-1} K^{-2} was found (slightly below that for $YNiSi_3$) yielding a jump of $\Delta C_{el}/\gamma_N T_c = 0.71(5)$ also below the value expected from BCS theory. The experimentally estimated Debye temperature was 474(8) K [$\beta = 0.0910(5)$ mJ mol^{-1} K^{-4} and $B = 0.000\,44(9)$ mJ mol^{-1} K^{-6}], similar to the previous work at high temperatures (484 K) [35]. The value of the electron-phonon coupling constant following Eq. (4) is $\lambda_{e\text{-}ph} = 0.44(2)$ also placing $LuNiSi_3$ in the weak-coupling regime. The density of states at the Fermi level is, following Eq. (3), $N(E_F) = 1.69$ states/eV f.u.

TABLE II. Fitted parameters of C_{el} in the superconducting region for $LuNiSi_3$. A_i, α, and a are dimensionless, Δ_0 is measured in 10^{-23} J, and γ_2 is measured in mJ mol^{-1} K^{-2}.

C_{el} model	A_i	Δ_0	f	γ_2	α'	a
SG	5.5(6)	2.6(2)				
DG	9.4(9)	1.1(1), 4.3(2)	0.10(1)			
SGNF	6.3(6)	3.7(2)		2.2(1)		
ANI	0.50(5)	5.0(2)			0.96(9)	0.62(6)

Figure 6(c) shows C_{el} vs T in the superconducting regime and fits using the models described in Eqs. (5) and (6). The fit parameters are given in Table II. The results are very similar to $YNiSi_3$, and it is not possible to determine which compound has a larger superconducting gap.

Resistivity measurements for $LuNiSi_3$ (Fig. 7) were conducted in the same configurations used for $YNiSi_3$. A sharp transition at 1.63(2) K takes place in zero field, and significant anisotropy is observed comparing Figs. 7(a) and 7(b) with the higher critical fields occurring for the geometry with $H \perp b$ in the same way as $YNiSi_3$. In Fig. 7(b), a complete transition occurs up to 80 mT. The residual resistivity before

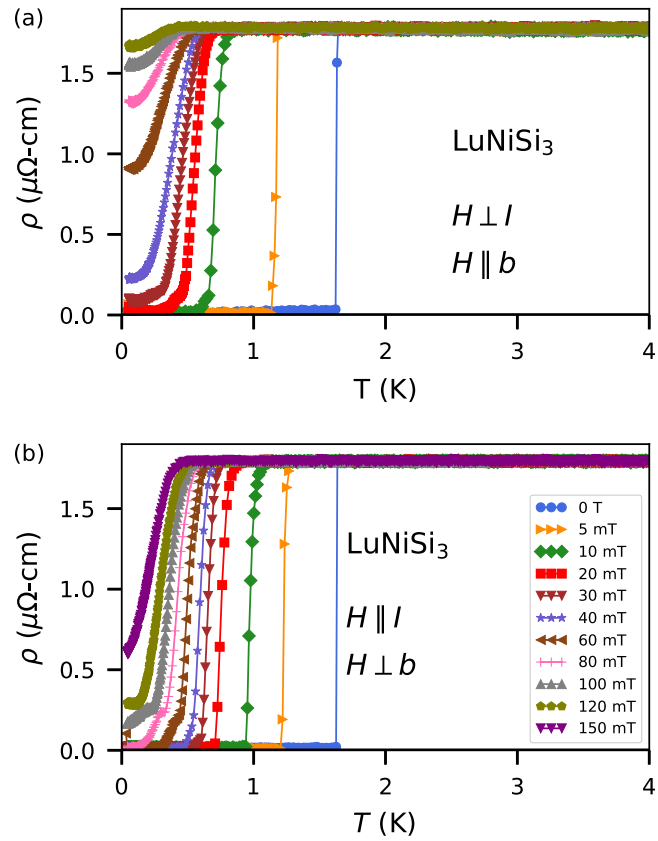

FIG. 7. Temperature dependence of the resistivity for $LuNiSi_3$ with H ranging from zero up to 0.15 T. (a) shows the configuration with $H \perp I$ and $H \parallel b$, and (b) shows the configuration with $H \parallel I$ and $H \perp b$.

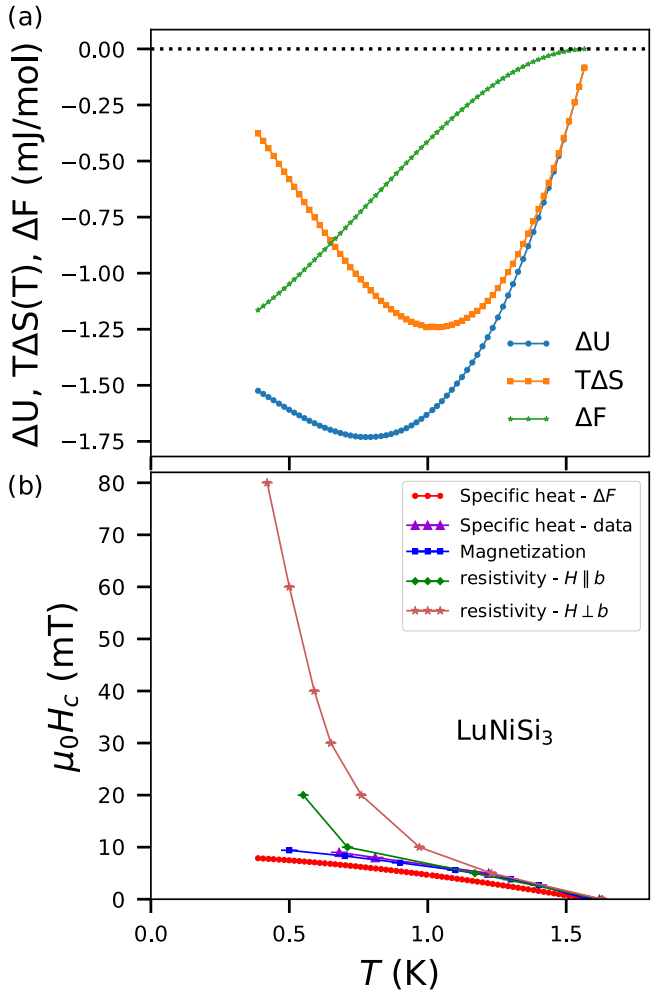

FIG. 8. (a) Temperature dependence of the internal energy difference (ΔU), latent heat ($T\ \Delta S$), and free energy (ΔF) for $LuNiSi_3$. These curves were calculated using the specific-heat measurements at zero field and Eq. (7). (b) Temperature dependence of the critical field $H_c(T)$ obtained from different techniques: using the free energy shown in (a) and using the specific-heat, magnetization, and resistivity measurements as a function of the applied field.

the superconducting transition for this compound is $\rho_0 = 1.8(3)\ \mu\Omega\,\text{cm}$ and RRR = 38(4) [35].

We performed the same thermodynamic analysis using Eq. (7) for $LuNiSi_3$, and results are displayed in Fig. 8(a). Overall, the energies and latent heat curves for both compounds are very similar but reach higher absolute values for $LuNiSi_3$. Figure 8(b) shows the $H_c(T)$ curve obtained using Eq. (7) and the data from Fig. 8(a) with a critical field of about 8.3 mT and the $H_c(T)$ curves obtained with the experimental results presented above. As for $YNiSi_3$, the $H_c(T)$ curves for $LuNiSi_3$ obtained from magnetization, specific heat, and resistivity with $H \parallel b$ are very similar, whereas the curve with $H \perp b$ in the resistivity gives much higher critical fields.

Following the same analysis used for $YNiSi_3$, the electron density of $LuNiSi_3$ yields $n = 3.83 \times 10^{28}\ \text{m}^{-3}$ with $V_{\text{cell}} = 313.62\ \text{Å}^3$ [35]. Assuming a spherical Fermi surface, the effective mass is $m^* = 1.51 m_0$ [the density of $LuNiSi_3$ is $6.5696(3)\ \text{g/cm}^3$], the estimated mean free path is equal to $l = 63$ nm, lower than for $YNiSi_3$, and the London penetration depth is 33(3) nm. Finally, the BCS coherence length in the clean limit is $\xi_0 = 690(70)$ nm, and using the equations above for λ_{GL} and ξ_{GL}, we obtain $\kappa = 0.42(4)$. This value also puts $LuNiSi_3$ in the type-I limit but much closer to the borderline value of 0.707.

IV. THEORETICAL RESULTS

Since Ni is commonly a magnetic ion, we first checked for the possibility of magnetic order by starting from different spin configurations [including Y(Lu) and Ni atoms with parallel spins, Y(Lu) and Ni atoms with antiparallel spins for each sublattice, etc.], but all starting configurations converged to a nonmagnetic ground state with zero local magnetic moments, i.e., diamagnetic compounds are obtained. These results are compatible with the magnetic measurements reported previously [35] and with the results presented in the Experimental Results section of this paper.

Having established the magnetic configuration of these compounds, we have studied their crystallographic properties. The crystal structure of $R\text{NiSi}_3$ has a base-centered orthorhombic centrosymmetric space-group *Cmmm* where the $R = (\text{Y}, \text{Lu})$ and the Ni atoms are located at the Wyckoff positions $4j$ ($m2m$) and $4i$ ($m2m$), respectively. There are three inequivalent Si atoms, two of them situated at positions $4i$ and one at $4j$. The crystal structure is shown in Fig. 9(a), and the calculated and experimental lattice constants are shown in Table I of the Supplemental Material [38]. The optimization of the Wyckoff positions and lattice vectors shows the same crystal symmetry for all calculated volumes. Comparing our results for the equilibrium volumes with the available experimental data, the absolute error for the lattice constants is less than 1% for both compounds, whereas absolute errors in the volume are 1.71% and 1.56% for $YNiSi_3$ and $LuNiSi_3$, respectively. Another important finding is deduced from the calculated vibrational dispersion relation at the equilibrium volumes where there are no imaginary frequencies, and therefore, the dynamical stability of the crystal structure of these compounds is maintained.

In order to understand the bonding properties of these crystalline materials, we have also calculated the ELF which gives a sound basis for a well-defined classification of bonds [50,51]. According to the ELF construction, this function can take values between 0 and 1, where 1 corresponds to perfect localization and 0.5 corresponds to the case of a homogeneous electron gas. Then, pure ionic bonding should manifest as high values of the ELF close to the nuclei and very low values ($\sim$0) uniformly distributed in the interstitial region. Pure covalent bonding between two atoms should display a local maximum of the ELF on the line connecting those atoms with a typical maximum value of the ELF in the range between 0.6 and 1.0, depending on how strong the bond is. Metallic bonding, which represents an intermediate case between the covalent bonding and ionic bonding, usually shows an almost uniform ELF distribution in the interstitial region with typical values on the order of 0.3–0.6. Figure 9(b) presents our calculated ELF for $YNiSi_3$. We have chosen three sections to display the ELF, namely, the $NiSi_2$ and YSi layers, i.e., the (001) and (002) planes, and a section through all three atoms: the (101) plane.

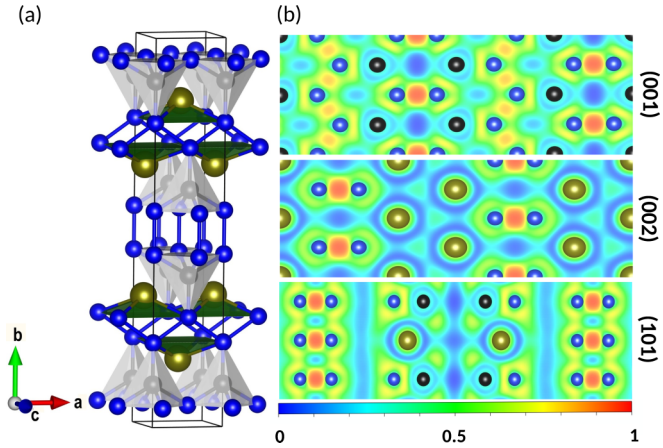

FIG. 9. (a) RNiSi$_3$ crystal structure, dark golden, black, and blue spheres denote the R, Ni, and Si atoms, respectively. The main building blocks are a set of corner-sharing square pyramids formed by Si that enclose the Ni atoms and another set of edge-sharing rectangular pyramids where the base and the apex are made up of Si and R atoms, respectively. Other remarkable features observed in this crystal structure are the pseudohexagons built up by Ni and Si atoms on (001) and the isosceles triangles made up by R atoms on (002). (b) Calculated electron localization function (ELF) for YNiSi$_3$; upper, middle, and bottom panels show the (001), (002), and (101) planes, respectively.

The ELF values on (001) indicate that the bond between the Si atoms forming dimers along [010] is covalent (maximum value of 0.95) and stronger than the also covalent bond (maximum value of 0.82) between the Si atoms that build up the zigzag chain along [100]. On the other hand, the ELF values found in the regions connecting Ni-Si atoms reveal the metallic character of these bonds (maximum value of 0.48). On the (002) plane, the ELF functions (maximum value of 0.95) corroborate the covalent nature of the bonds of the Si dimers along [010], whereas the bonding between the Y and the Si atoms is metallic (maximum value of 0.51). Observing the ELF between the Y atoms that build the isosceles triangle on (002), we can deduce the bonding is ionic (maximum value of 0.21). Finally, the calculated ELF on (101) shows the weakly metallic behavior of the Y-Ni bond (maximum value of 0.32). To summarize, all types of chemical bonds can be distinguished in the YNiSi$_3$ system: ionic (between Y atoms), metallic (among Ni-Si, Y-Si, and Ni-Y), and covalent (within the Si dimers and zigzag chains). We do not show the calculated ELF for LuNiSi$_3$ because it is very similar to YNiSi$_3$ and, consequently, the bonding properties are the same.

We have also calculated the elastic constants (see Table II of the Supplemental Material [38]) and then the Debye temperature using the following equation:

$$\Theta_D = \frac{\hbar s q_D}{k_B}, \tag{8}$$

where $s = \left(\frac{1}{3s_l^3} + \frac{2}{3s_t^3}\right)^{-1/3}$ is the average sound velocity, $s_l = \sqrt{\frac{B+\frac{4}{3}G}{\rho}}$ is the longitudinal sound velocity, $s_t = \sqrt{\frac{G}{\rho}}$ is the transverse sound velocity, G is the isotropic shear modulus which is calculated in terms of the crystalline lattice constants $q_D = \sqrt[3]{6\pi^2\eta_\alpha}$, and η_α is the atomic concentration. The calculated values are 497 and 464 K for YNiSi$_3$ and LuNiSi$_3$ with absolute relative errors of 6.7 and 2.1%, in good agreement with the experimental values.

For a better understanding of the basic electronic properties that may lead to the experimentally observed behavior of YNiSi$_3$ and LuNiSi$_3$, we now present the calculated DFT electronic structure for both compounds. Figure 10 displays the calculated dispersion relations along the high-symmetry directions of the first Brillouin zone (FBZ) and the total and projected DOS for both compounds for one spin direction. The YNiSi$_3$ valence bands are composed of Ni d states for the most part, a small contribution of Si p states, and an even smaller contribution of Y d states [Fig. 10(a)]. The valence bands of LuNiSi$_3$ are similar to those of YNiSi$_3$, although the presence of Lu f states introduce almost dispersionless bands around 4.1 and 5.6 eV below the Fermi level [Fig. 10(b)]. The splitting of the f bands (1.5 eV) is due to the spin-orbit coupling that, in the case of LuNiSi$_3$, is much stronger than the crystal-field splitting which lifts all the degeneracies of the Lu f states (point-group $m2m$) by less than 5 meV. The LuNiSi$_3$ upper valence bands are composed mainly of Ni d states and some contribution of Si p and Lu d states. The conduction bands are also the result of the hybridization of d states coming from the metallic atoms with the Si p states, and for energies larger than 1 eV the contribution of Si s states becomes relevant as well. At the Fermi level, the contributions of the projected DOS for YNiSi$_3$ are (in states/f.u., spin, and eV) 0.2131, 0.2544, and 0.1719 for Y d, Ni d, and Si p states, respectively. In the case of LuNiSi$_3$, the contributions at the Fermi level of the Lu d, Ni d, and Si p states are 0.223, 0.2676, and 0.1858. Thus, we would expect an important contribution of $3d$, $3p$, and $4d$ orbitals in the superconductivity of YNiSi$_3$ ($3d$, $3p$, and $5d$ orbitals for LuNiSi$_3$).

We have also estimated, under the crude assumption of the Sommerfeld model, the bare specific-heat coefficient $\gamma_{\text{bare}} = \frac{2}{3}\pi^2\eta_F k_B^2$, where η_F is the total DOS at the Fermi level (in states/f.u., spin, and eV). We have obtained for YNiSi$_3$ and LuNiSi$_3$, respectively, $\eta_F = 0.6875$ and 0.7433 (the relative errors are 19.6% and 12%), given $\gamma_{\text{bare}} = 3.24$ and 3.50 mJ mol^{-1} K^{-2}. Furthermore, we have estimated the specific-heat enhancement $\frac{\gamma_{\text{exp}}}{\gamma_{\text{bare}}} = (1 + \lambda_{\text{e-ph}})$, obtaining $\lambda_{\text{e-ph}} = 0.247$ and 0.134 for YNiSi$_3$ and LuNiSi$_3$, respectively. Such values for the electron-phonon coupling confirm that these compounds are in the weak-coupling regime.

The topology of the three conduction bands crossing the Fermi level is almost identical for both compounds as shown in Fig. 10 [FBZ high-symmetry points and directions are shown in Fig. 11(a)]. The first partially occupied band (magenta line) crosses the Fermi level in the vicinity of the high-symmetry point T, and it has a holelike character, its atomic character [see the inset in Fig. 10(a)] is built up by Ni d and Si p states. The second conduction band (violet line) crosses the Fermi level in all the high-symmetry directions except the Δ direction (k_y). This band has an appreciable dispersion in all the directions that it crosses where its holelike character is manifested in the Λ, H, T-Γ, Γ-S, and D directions. This band is made up by the hybridization of Y (Lu) d, Ni d, and Si p states except in the D direction where only the Ni and

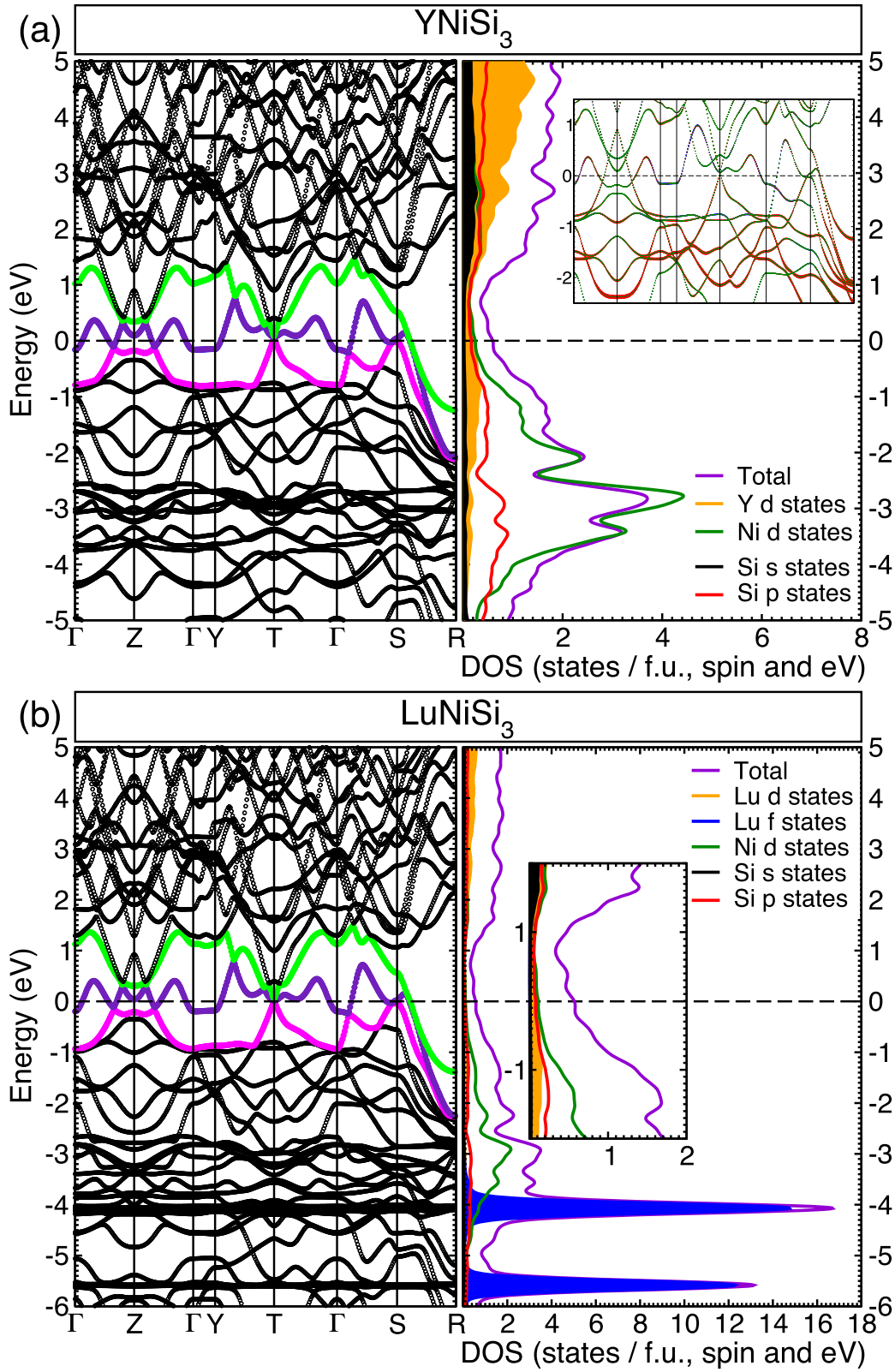

FIG. 10. Calculated electronic structure: dispersion relation, total, and projected DOS for (a) $YNiSi_3$ and (b) $LuNiSi_3$. Highlighted in color are the three conduction bands crossing the Fermi level; band 1 (magenta), band 2 (violet), and band 3 (green). The eigenvalues are shifted to the Fermi level, which is indicated by a dashed line. The inset in panel (a) shows the atomic character of the dispersion relation where thick blue, red, and green lines correspond to Y d, Ni d, and Si p states, respectively. The inset in panel (b) zooms in on the projected DOS contributions at the Fermi level.

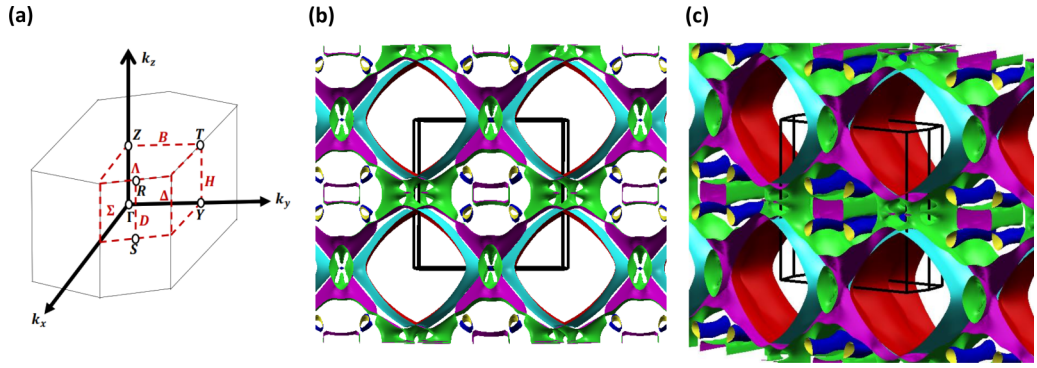

FIG. 11. (a) FBZ of the space-group *Cmmm*. The main symmetry points and lines are labeled in black and red, respectively. (b) Extended Fermi surface of $YNiSi_3$. The FBZ is shown by black lines, and it is oriented along the Δ direction (k_y). (c) Extended Fermi surface of $LuNiSi_3$.

Si orbitals are present. On the other hand, the third partially occupied band (green line) crosses only the D direction, having large dispersion and electron character. The orbital character of this band is only due to Ni d and Si p states. As was previously suggested [52] and later measured [34] for $YbNiSi_3$, the three bands collectively indicate that these compounds are good conductors along the [100] and [001] crystallographic directions but not along [010]. Our electronic structure results for both compounds also demonstrate their similarity to the isostructural compound $YNiGe_3$ [29].

Figure 11 provides a visual representation of the calculated FS of these compounds. The first hole branch is formed by four pipes (blue/yellow surfaces) centered around Γ and parallel to the Δ direction. The second branch has two main features, a holelike rectangular cylinder (green/violet colors) also centered around Γ and with its axis oriented along the Δ direction and a set of large holelike cylinders running along the FBZ boundary, parallel to the Δ direction and intricately connected around the FBZ boundaries. The third branch is built by four large electronlike disconnected cylinders (cyan/red colors) centered around the edge of the FBZ and running parallel to the Δ direction. The first hole and the electron branches result from the hybridization of Ni d with Si p states, whereas the second hole branch also has the contribution of Y (Lu) d orbitals. Thus, the two large cylindrical branches are most likely responsible for the observed superconductivity in these systems.

Finally, we have also calculated the phononic properties of these compounds, such as the phonon dispersion relation, the partial density of states $F(\omega)$, and the spectrum function $\omega^{-2}F(\omega)$. We did not include the SOC in the calculation of the vibrational properties because the crystal structure and the FS are not affected by this interaction. The primitive cell of these systems contains ten atoms; therefore the phonon spectrum contains 3 acoustic and 27 optical branches as shown in Fig. 12. Although the dispersion relation and partial $F(\omega)$ show an almost continuous distribution of modes across the whole frequency range, we can divide the phonon spectrum into three frequency regions: acoustic (0–4.0 and 0–3.2 THz for $YNiSi_3$ and $LuNiSi_3$, respectively), intermediate (4.0–12.2 and 2.6–12.8 THz), and high (12.2–14.5 and 12.8–14.6 THz). The acoustic branches are made up from states of all the atoms almost evenly for $YNiSi_3$, whereas there is an appreciable increment of the Lu contribution in the case of $LuNiSi_3$ due to its heavy mass. The intermediate-frequency range has 23 branches where 12 of these (up to approximately 6.7 THz) form the low-lying optical branches. These 12 branches are built up by states coming from all the atoms with Y (Lu) and Si contributions being larger than the Ni one. The remaining 11 intermediate branches are mainly made up of Si contributions and a small contribution of Ni states. The four branches forming the high-frequency region are almost solely formed by Si contributions.

From $F(\omega)$, we can also obtain the spectrum function $\omega^{-2}F(\omega)$, that can be used as a crude alternative to the Eliashberg function $\alpha^2F(\omega)$; these two spectral functions exhibit a similar peak structure [53]. We can observe that $\omega^{-2}F(\omega)$ has its larger spectral weight in the acoustical and low-lying optical branches for both compounds with its more prominent peaks located around the latter as is shown in Fig. 12. These 12 branches have contributions from the vibrations of all atoms [Y(Lu), Ni, Si], indicating that the coupling between the d electrons from Y(Lu) and Ni to Si p electrons will form Cooper pairs, therefore, they are responsible for the observed superconductivity of these compounds.

V. DISCUSSION

To summarize, both $YNiSi_3$ and $LuNiSi_3$ present bulk superconductivity, showing the features of type-I superconductors with $\kappa = 0.113(11)$ for $YNiSi_3$ and $\kappa = 0.42(4)$ for $LuNiSi_3$. The main superconducting parameters for both compounds are given in Table III.

The discovery of type-I superconductivity in ternary compounds is not unprecedented with recent publications reporting the appearance of type-I superconductivity in the cage compound $LaTi_2Al_{20}$ [11] and in the NCS $LaPdSi_3$ [12] and $LaIrSi_3$ [13] compounds. The case of the NCS $LaRhSi_3$ is even more intriguing since it has been recently reported as a type-II/1 superconductor with $\kappa = 0.25$ [24,26]. This compound has a phase diagram with resistivity and susceptibility measurements giving an exceptionally high upper critical field (≈120 mT) compared to $H_c(0)$ obtained from standard specific-heat and magnetization measurements (≈20 mT), interpreted as arising from surface superconductivity.

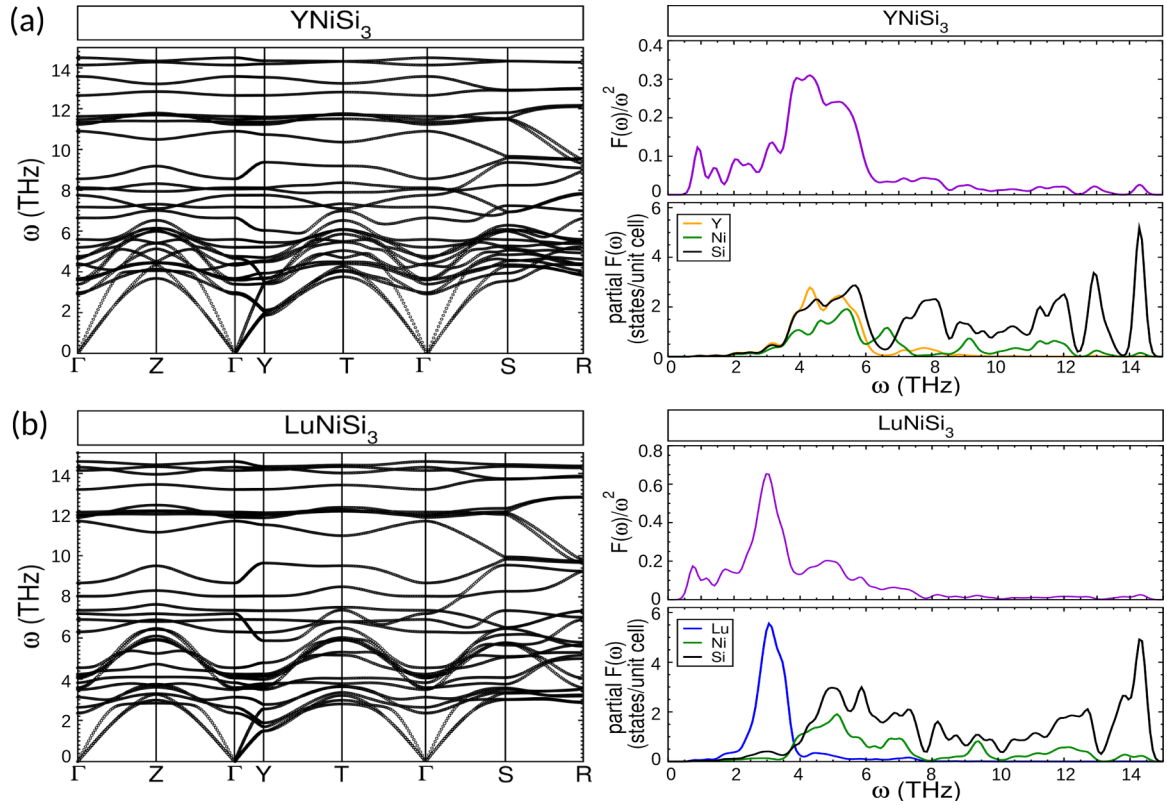

FIG. 12. Calculated phonon dispersion relation and $F(\omega)/\omega^2$ and partial density of states $F(\omega)$ for (a) $YNiSi_3$ and (b) $LuNiSi_3$.

DFT results show that both $YNiSi_3$ and $LuNiSi_3$ have a nonmagnetic ground state and that, although SOC does not affect the FS of these compounds, SOC does act significantly on the Lu f states below the Fermi level resulting in a large splitting of these orbitals that overcomes the insignificant crystal-field splitting. ELF shows that for both compounds there are three types of atomic bonding: metallic, covalent, and ionic. The metallic bond is observed between Lu(Y) and Si on the (002) plane and the Ni and Si atoms on the (001) plane. The electronic structure indicates that these compounds are good conductors along the [100] and [001] directions but not along [010]. From the FS, we find that the second hole branch is built up by hybridization of Y(Lu) d, Ni d, and Si p states, whereas Ni d and Si p states hybridize to form the electron branch. These branches connect the FBZ boundaries and are responsible for the observed superconductivity. The partial $F(\omega)$ and spectrum function $\omega^{-2}F(\omega)$ indicate that the coupling of Y(Lu), Ni d, and Si p electrons in the low-lying optical phonon branches will form the Cooper pairs responsible of the superconducting state. These findings show that these compounds are anisotropic three-dimensional (3D) metals with a multiband superconducting state.

The larger spectral weight $\omega^{-2}F(\omega)$ present in $LuNiSi_3$ for the low-lying optical branches together with the large η_F might explain the higher critical temperature seen in $LuNiSi_3$.

TABLE III. Experimental superconducting parameters for $YNiSi_3$ and $LuNiSi_3$. The value of $H_c(0)$ was estimated from the magnetization measurements.

	$YNiSi_3$	$LuNiSi_3$
T_c (K)	1.36(3)	1.61(2)
γ_N (mJ mol^{-1} K^{-2})	4.04(9)	3.97(9)
θ_D (K)	466(9)	474(8)
$\lambda_{e\text{-}ph}$	0.43(2)	0.44(2)
$\Delta C_{el}/\gamma_N T_c$	1.14(9)	0.71(5)
$\mu_0 H_c(0)$ (mT)	9.6(2)	10.4(2)
λ_L (nm)	34(3)	33(3)
ξ_0 (nm)	780(80)	690(70)
κ	0.113(11)	0.42(4)

VI. CONCLUSION

We have reported the discovery of superconductivity in $YNiSi_3$ [$T_c = 1.36(3)$ K] and $LuNiSi_3$ [$T_c = 1.61(2)$ K] by characterizing the superconducting behaviors of single crystals through magnetization, heat-capacity, and resistivity experiments with support from DFT band-structure calculations. Both compounds show bulk superconductivity with features that are typical of type-I SC but with a low jump in the specific heat [$\Delta C_{el}/\gamma_n T_c$ is equal to 1.14(9) and 0.71(5) for the Y and Lu compounds, respectively]. Resistivity measurements show a highly anisotropic behavior between the measurements under an applied field with the configuration $H \perp b$ displaying the highest critical fields. DFT calculations show that these compounds are anisotropic 3D metals with a multiband superconducting ground state.

ACKNOWLEDGMENTS

The authors acknowledge financial support from Brazilian funding agencies CAPES, CNPq, and FAPESP (Contracts No. 2011/19924-2, No. 2012/17562-9, No. 2014/20365-6, and No. 2017/01827-7), Colombian agency COLCIENCIAS (Convocatoria Doctorados Nacionales No. 757 de 2016), and Vicerrectoría de Investigación Universidad de Antioquia Estrategia de Sostenibilidad No. 2018-2019 (Colombia). We also acknowledge fruitful discussions with G. Eguchi and J. Sereni.

[1] F. Kneidinger, E. Bauer, I. Zeiringer, P. Rogl, C. Blaas-Schenner, D. Reith, and R. Podloucky, Physica C (Amsterdam) **514**, 388 (2015).

[2] J. Bardeen, L. N. Cooper, and J. R. Schrieffer, Phys. Rev. **106**, 162 (1957).

[3] M. R. Norman, Science **332**, 196 (2011).

[4] T. Das and C. Panagopoulos, New J. Phys. **18**, 103033 (2016).

[5] M. Smidman, M. B. Salamon, H. Q. Yuan, and D. F. Agterberg, Rep. Prog. Phys. **80**, 036501 (2017).

[6] M. J. Winiarski, B. Wiendlocha, S. Gołab, S. K. Kushwaha, P. Wiśniewski, D. Kaczorowski, J. D. Thompson, R. J. Cava, and T. Klimczuk, Phys. Chem. Chem. Phys. **18**, 21737 (2016).

[7] S. Sun, K. Liu, and H. Lei, J. Phys.: Condens. Matter **28**, 085701 (2016).

[8] E. Svanidze and E. Morosan, Phys. Rev. B **85**, 174514 (2012).

[9] L. L. Zhao, S. Lausberg, H. Kim, M. A. Tanatar, M. Brando, R. Prozorov, and E. Morosan, Phys. Rev. B **85**, 214526 (2012).

[10] H. Leng, C. Paulsen, Y. K. Huang, and A. de Visser, Phys. Rev. B **96**, 220506(R) (2017).

[11] A. Yamada, R. Higashinaka, T. D. Matsuda, and Y. Aoki, J. Phys. Soc. Jpn. **87**, 033707 (2018).

[12] M. Smidman, A. D. Hillier, D. T. Adroja, M. R. Lees, V. K. Anand, R. P. Singh, R. I. Smith, D. M. Paul, and G. Balakrishnan, Phys. Rev. B **89**, 094509 (2014).

[13] V. K. Anand, D. Britz, A. Bhattacharyya, D. T. Adroja, A. D. Hillier, A. M. Strydom, W. Kockelmann, B. D. Rainford, and K. A. McEwen, Phys. Rev. B **90**, 014513 (2014).

[14] J. Auer and H. Ullmaier, Phys. Rev. B **7**, 136 (1973).

[15] V. Moshchalkov, M. Menghini, T. Nishio, Q. H. Chen, A. V. Silhanek, V. H. Dao, L. F. Chibotaru, N. D. Zhigadlo, and J. Karpinski, Phys. Rev. Lett. **102**, 117001 (2009).

[16] E. Babaev, J. Carlström, M. Silaev, and J. M. Speight, Physica C (Amsterdam) **533**, 20 (2017).

[17] T. Bauch, E. Babaev, M. G. Blamire, C. Brun, A. Buzdin, J. Carlström, T. Cren, O. Dobrovolskiy, J. Ge, V. N. Gladilin *et al.*, *Superconductors at the Nanoscale: From Basic Research to Applications* (de Gruyter, Berlin, 2017).

[18] T. Reimann, M. Schulz, D. F. R. Mildner, M. Bleuel, A. Brûlet, R. P. Harti, G. Benka, A. Bauer, P. Böni, and S. Mühlbauer, Phys. Rev. B **96**, 144506 (2017).

[19] Y. Wang, R. Lortz, Y. Paderno, V. Filippov, S. Abe, U. Tutsch, and A. Junod, Phys. Rev. B **72**, 024548 (2005).

[20] J.-Y. Ge, J. Gutierrez, A. Lyashchenko, V. Filipov, J. Li, and V. V. Moshchalkov, Phys. Rev. B **90**, 184511 (2014).

[21] D. J. Rebar, Exploring Superconductivity in Chiral Structured AuBe, Ph.D. thesis, Louisiana State University and Agricultural and Mechanical College, 2015.

[22] A. V. Tsvyashchenko, V. A. Sidorov, A. E. Petrova, L. N. Fomicheva, I. P. Zibrov, and V. E. Dmitrienko, J. Alloys Compd. **686**, 431 (2016).

[23] P. Lejay, I. Higashi, B. Chevalier, J. Etourneau, and P. Hagenmuller, Mater. Res. Bull. **19**, 115 (1984).

[24] V. K. Anand, A. D. Hillier, D. T. Adroja, A. M. Strydom, H. Michor, K. A. McEwen, and B. D. Rainford, Phys. Rev. B **83**, 064522 (2011).

[25] N. Kimura, H. Ogi, K. Satoh, G. Ohsaki, K. Saitoh, H. Iida, and H. Aoki, JPS Conf. Proc. **3**, 01501-1 (2014).

[26] N. Kimura, N. Kabeya, K. Saitoh, K. Satoh, H. Ogi, K. Ohsaki, and H. Aoki, J. Phys. Soc. Jpn. **85**, 024715 (2016).

[27] S. J. Ray, A. S. Gibbs, S. J. Bending, P. J. Curran, E. Babaev, C. Baines, A. P. Mackenzie, and S. L. Lee, Phys. Rev. B **89**, 094504 (2014).

[28] E. D. Mun, S. L. Bud'ko, H. Ko, G. J. Miller, and P. C. Canfield, J. Magn. Magn. Mater. **322**, 3527 (2010).

[29] M. J. Winiarski and M. Samsel-Czekała, Solid State Commun. **179**, 6 (2014).

[30] A. P. Pikul and D. Gnida, Solid State Commun. **151**, 778 (2011).

[31] M. Nakashima, K. Tabata, A. Thamizhavel, T. C. Kobayashi, M. Hedo, Y. Uwatoko, K. Shimizu, R. Settai, and Y. Ōnuki, J. Phys.: Condens. Matter **16**, L255 (2004).

[32] H. Kotegawa, K. Takeda, T. Miyoshi, S. Fukushima, H. Hidaka, T. C. Kobayashi, T. Akazawa, Y. Ohishi, M. Nakashima, A. Thamizhavel *et al.*, J. Phys. Soc. Jpn. **75**, 044713 (2006).

[33] E. D. Mun, S. L. Bud'ko, A. Kreyssig, and P. C. Canfield, Phys. Rev. B **82**, 054424 (2010).

[34] M. A. Avila, M. Sera, and T. Takabatake, Phys. Rev. B **70**, 100409(R) (2004).

[35] F. R. Arantes, D. Aristizábal-Giraldo, S. H. Masunaga, F. N. Costa, F. F. Ferreira, T. Takabatake, L. Mendonça-Ferreira, R. A. Ribeiro, and M. A. Avila, Phys. Rev. Mater. **2**, 044402 (2018).

[36] K. Dewhurst, S. Sharma, L. Nordstrom, F. Cricchio, F. Bultmark, H. Gross, C. Ambrosch-Draxl, C. Persson, C. Brouder, R. Armiento *et al.*, ELK [http://elk.sourceforge.net] (2016).

[37] J. P. Perdew, A. Ruzsinszky, G. I. Csonka, O. A. Vydrov, G. E. Scuseria, L. A. Constantin, X. Zhou, and K. Burke, Phys. Rev. Lett. **100**, 136406 (2008).

[38] See Supplemental Material at http://link.aps.org/supplemental/10.1103/PhysRevB.99.224505 for the tables with the lattice parameters and the elastic module.

[39] S. P. Murarka, *Silicides for VLSI Applications* (Academic Press, New York, 2012).

[40] M. K. Niranjan, V. S. Kumar, and R. Karthikeyan, J. Phys. D **47**, 285101 (2014).

[41] J.-Y. Lin, H.-M. Hsu, and K.-C. Lu, CrystEngComm **17**, 1911 (2015).

[42] M. Tinkham, *Introduction to Superconductivity* (McGraw-Hill, New York, 1996).

[43] W. L. McMillan, Phys. Rev. **167**, 331 (1968).

[44] V. H. Tran and M. Sahakyan, Sci. Rep. **7**, 15769 (2017).
[45] M. Sahakyan and V. H. Tran, J. Phys.: Condens. Matter **28**, 205701 (2016).
[46] G.-Y. Chen, X. Zhu, H. Yang, and H.-H. Wen, Phys. Rev. B **96**, 064524 (2017).
[47] F. Gross, B. S. Chandrasekhar, D. Einzel, K. Andres, P. J. Hirschfeld, H. R. Ott, J. Beuers, Z. Fisk, and J. L. Smith, Z. Phys. B **64**, 175 (1986).
[48] R. Ribeiro-Palau, R. Caraballo, P. Rogl, E. Bauer, and I. Bonalde, J. Phys.: Condens. Matter **26**, 235701 (2014).
[49] J. R. Waldram, *Superconductors of Metals and Cuprates* (Institute of Physics Publishing, Bristol, 1996).
[50] A. D. Becke and K. E. Edgecombe, J. Chem. Phys. **92**, 5397 (1990).
[51] A. Savin, R. Nesper, S. Wengert, and T. F. Fässler, Angew. Chem., Int. Ed. Engl. **36**, 1808 (1997).
[52] G.-H. Sung and D.-B. Kang, Bull. Korean Chem. Soc. **24**, 325 (2003).
[53] A. Junod, D. Bichsel, and J. Muller, Helvetica Physica Acta **52**, 580 (1979).